Original Article

MOLECULAR METABOLISM

The BBSome regulates mitochondria dynamics and function

Deng-Fu Guo [1,2], Ronald A. Merrill [1], Lan Qian [3], Ying Hsu [2], Qihong Zhang [4], Zhihong Lin [1], Daniel R. Thedens [5], Yuriy M. Usachev [1], Isabella Grumbach [2,3,6], Val C. Sheffield [4,6,7], Stefan Strack [1,6,7], Kamal Rahmouni [1,2,3,6,7,8,*]

ABSTRACT

Objective: The essential role of mitochondria in regulation of metabolic function and other physiological processes has garnered enormous interest in understanding the mechanisms controlling the function of this organelle. We assessed the role of the BBSome, a protein complex composed of eight Bardet-Biedl syndrome (BBS) proteins, in the control of mitochondria dynamic and function.

Methods: We used a multidisciplinary approach that include CRISPR/Cas9 technology-mediated generation of a stable *Bbs1* gene knockout hypothalamic N39 neuronal cell line. We also analyzed the phenotype of BBSome deficient mice in presence or absence of the gene encoding A-kinase anchoring protein 1 (AKAP1).

Results: Our data show that the BBSome play an important role in the regulation of mitochondria dynamics and function. Disruption of the BBSome cause mitochondria hyperfusion in cell lines, fibroblasts derived from patients as well as in hypothalamic neurons and brown adipocytes of mice. The morphological changes in mitochondria translate into functional abnormalities as indicated by the reduced oxygen consumption rate and altered mitochondrial distribution and calcium handling. Mechanistically, we demonstrate that the BBSome modulates the activity of dynamin-like protein 1 (DRP1), a key regulator of mitochondrial fission, by regulating its phosphorylation and translocation to the mitochondria. Notably, rescuing the decrease in DRP1 activity through deletion of one copy of the gene encoding AKAP1 was effective to normalize the defects in mitochondrial morphology and activity induced by BBSome deficiency. Importantly, this was associated with improvement in several of the phenotypes caused by loss of the BBSome such as the neuroanatomical abnormalities, metabolic alterations and obesity highlighting the importance of mitochondria defects in the pathophysiology of BBS.

Conclusions: These findings demonstrate a critical role of the BBSome in the modulation of mitochondria function and point to mitochondrial defects as a key disease mechanism in BBS.

Keywords Mitochondria; Bardet-biedl syndrome proteins; Body weight; Leptin sensitivity

1. INTRODUCTION

Mitochondria are best known as the powerhouse of the cell and critical determinants of energy metabolism through the generation of ATP. The importance of mitochondria extends beyond the conversion of energy due to its involvement in the regulation of a wide range of cellular processes such as reactive oxygen species, intracellular calcium handling, differentiation, proliferation, and survival [1,2]. Of note, dysregulation in these mitochondria regulated processes underlies a vast array of health problems including metabolic and neuropsychological diseases [3–6]. Thus, therapeutic agents that restore mitochondria health may be beneficial in the treatment of these diseases [7].

Mitochondria are highly dynamic, adjusting their functions to the changing metabolic demands and cellular stress by migrating throughout the cell and undergoing regulated turnover and morphological changes through fission and fusion [8,9]. Mitochondria fusion requires mitofusin 1 (MFN1) and MFN2 located in the outer membrane and optic atrophy 1 (OPA1), a mitochondrial dynamin like GTPase in the inner mitochondrial membrane [10,11]. In contrast, fission is catalyzed by dynamin-like protein 1 (DPR1) which is targeted to the outer membrane through interaction with mitochondrial fission factor (MFF) [12]. The enzymatic activity of DRP1 is determined by phosphorylation at several sites, of which Ser616 phosphorylation enhances DRP1 function, whereas Ser637 phosphorylation inhibits DRP1 activity [6,13]. A-kinase anchoring protein 1 (AKAP1) is a mitochondrial

[1]Department of Neuroscience and Pharmacology, University of Iowa Carver College of Medicine, Iowa City, IA, USA [2]Veterans Affairs Health Care System, Iowa City, IA, USA [3]Department of Internal Medicine, University of Iowa Carver College of Medicine, Iowa City, IA, USA [4]Department of Pediatrics, University of Iowa Carver College of Medicine, Iowa City, IA, USA [5]Department of Radiology, University of Iowa Carver College of Medicine, Iowa City, IA, USA [6]Fraternal Order of Eagles Diabetes Research Center, University of Iowa Carver College of Medicine, Iowa City, IA, USA [7]Iowa Neuroscience Institute, University of Iowa Carver College of Medicine, Iowa City, IA, USA [8]Obesity Research and Education Initiative, University of Iowa Carver College of Medicine, Iowa City, IA, USA

*Corresponding author. Department of Neuroscience and Pharmacology, University of Iowa Carver College of Medicine, Iowa City, IA, 52242, USA. E-mail: kamal-rahmouni@uiowa.edu (K. Rahmouni).

Received October 21, 2022 • Accepted December 6, 2022 • Available online 10 December 2022

Non-standard Abbreviations

AAV	adeno-associated virus
Adipo	adiponectin
AKAP1	A-kinase anchoring protein 1
AgRP	agouti-related protein
BBS	Bardet-Biedl syndrome
CHC	clathrin heavy chain
DPR1	dynamin-like protein 1
ERG	electroretinography
MCU	calcium uniporter
MFF	mitochondrial fission factor
MFN1 and 2	mitofusin 1 and 2
MRI	magnetic resonance imaging
POMC	proopiomelanocortin
OPA1	optic atrophy 1
PDGF-BB	platelet derived growth factor-BB
PKA	protein kinase A
RFP	red fluorescent protein
STAT3	signal transducer and activator of transcription 3
TEM	transmission electron microscopy

scaffold protein that promote protein kinase A (PKA)-mediated phosphorylation of DRP1(Ser637) by increasing the local concentration of PKA at the outer mitochondrial membrane [14,15]. However, our understanding of the molecular machinery that regulates mitochondria dynamic and function remains far from complete.

The BBSome which was identified in 2007 is a heterooctameric protein complex of eight Bardet-Biedl syndrome (BBS) proteins (BBS1, BBS2, BBS4, BBS5, BBS7, BBS8, BBS9, and BBS18) [16]. The BBSome contains coat-like structural elements common to COPI, COPII, and clathrin coats and is the major effector of the Arf-like GTPase Arl6/BBS3, another highly conserved BBS protein [17]. Assembly of the BBSome depends on another protein complex that contain three BBS proteins (BBS6, BBS10, BBS12). Dysfunction of the BBSome following loss of any of its proteins or other components required for its formation or function causes BBS, a multiorgan disorder characterized by various phenotypes including obesity, visual impairment caused by retinal degeneration, hypogonadism, hydrocephalus and other neurological problems [18,19].

The BBSome was initially thought to be exclusively associated with the function of cilia, a hair like structure present in virtually every cell in the body, by mediating the trafficking of cargos to and from the ciliary membrane. However, the BBSome has now been implicated in the regulation of several other cellular processes including the sorting of receptors to the plasma membrane, gene expression and proteasomal activity [20]. For instance, the requirement of the BBSome for the plasma membrane localization of key receptors underlying energy homeostasis such as the leptin receptor explain the obesity and hyperphagia evoked by BBSome disruption [21–23].

Here, we identified a novel role for the BBSome in the regulation of mitochondria dynamics and function. We found that a functional BBSome is required for proper mitochondria morphology as indicated by the elongated mitochondria in cells lacking a functional BBSome. The morphological changes in the mitochondria evoked by loss of the BBSome are associated with alterations in mitochondrial activity. We identified a reduction in DRP1 activity as a mediator of the mitochondrial dysfunction evoked by BBSome deficiency. Importantly, rescuing the decrease in DRP1 activity through *Akap1* gene heterozygosity improved several of the phenotypes induced by disruption of the BBSome.

2. MATERIAL AND METHODS

2.1. Constructs and antibodies

pSpCas9-Bbs1g2 was used for creating N39 and IMCD3 *Bbs1* knockout *(Bbs1*KO) cells. RFG-tagged BBS7, was reported previously [24]. Red fluorescent protein (RFP)-tagged BBS7 was created by insertion of cherry red fluorescence 5' of each gene in pcDNA3.1 mammalian expression vector. mtRGECO was used to measure mitochondria Ca^{2+} intake as described below. All antibodies information used in this study are listed in the Supplemental Table S1 with their dilution indicated below.

2.2. Animals

All animal testing was performed based on guidelines set forth by the National Institutes of Health and approved by The University of Iowa Animal Care and Use Committee. Mice were housed in groups of 3—5 per cage and maintained on 12-h light—dark cycle with lights on at 6 am. Room temperature was maintained at 22 °C. Food and water were available *ad libitum* except when the mice were fasted.

Male and female *Akap1*$^{-/-}$ mice [25], *Bbs4*$^{-/-}$ [26] and *Bbs8*$^{-/-}$ mice [27] from our colonies were used. *Akap1*$^{-/-}$ mice were bred with *Bbs8*$^{+/-}$ mice to generate *Akap1*$^{+/+}$/*Bbs8*$^{-/-}$ and *Akap1*$^{+/-}$/*Bbs8*$^{-/-}$ mice and their controls (*Akap*$^{+/+}$/*Bbs8*$^{+/+}$). Proopiomelanocortin (POMC)$^{Cre/}$*Bbs1*$^{fl/fl}$ mice and adiponectin (Adipo)^{Cre}/*Bbs1*$^{fl/fl}$ mice were generated by crossing the *Bbs1*$^{fl/fl}$ mice with POMC^{Cre} mice and Adipo^{Cre} mice, respectively, as reported previously [21,22]. The genotype of the mice was determined by PCR analysis of tail DNA using the following conditions: 95 °C for 30 s, 60 °C for 30 s, and 72 °C for 30 s for a total of 34 cycles Primers used for genotyping were listed in Supplemental Table S1.

2.3. Generation and analysis of *Bbs1*KO cell lines

The human codon-optimized Cas9 plasmid pX459 (Addgene # 48139) was obtained from Addgene. sgRNAs were designed and constructed as described previously [22]. Briefly, target 20 bp sequences starting with guanine and preceding the PAM motif (5′-NGG-3′) were selected from mouse *Bbs1* exon 4. Potential off-target effects of sgRNA candidates were analyzed using the online tool CRISPR Design developed by Zhang's laboratory (http://crispr.mit.edu/). One sgRNA in exon 4 (Supplemental Table S1) of the mouse *Bbs1* gene was selected for transfection to create knockout cell lines. Clonal genomic DNA was extracted and used for PCR and Sanger sequencing with the forward primer and the reverse primer (Supplemental Table S1). This resulted in cell lines with homozygous 1 bp T insertions and homozygous 2bp deletions (del CT) in exon 4.

In the pDRP1 rescue experiments, the cells were infected with an adeno-associated virus expressing a mouse BBS1 protein (AAV-*Bbs1*) [28] or a feline immunodeficiency virus expressing a mutant from of rat DRP1 (FIV-DRP1S637A) [13,25] (1000 per cell) for 48 h. It is worth noting that FIV-DRP1S637A expresses an shRNA that reduces endogenous DRP1 expression. To activate PKA, cells were exposed to 20 μM forskolin for 1 h.

Mouse hypothalamic N39 cells and mouse kidney epithelial IMCD3 cells (mIMCC-3, ATCC# CRL-2123) were cultured in DMEM/F12 and DMEM respectively (Life Technologies) supplemented with 10% FBS. Cells were seeded in a 6-well plate at 1×10^6 cells/well. Transfection was performed with Lipofectamine 2000 following the manufacturer's instructions. Briefly, 2 μg of plasmid containing a sgRNA targeting *Bbs1* exon 4 and 6 μl Lipofectamine 2000 were diluted in 100 μl Opti-MEM, mixed 1:1 and added to cells after 15 min incubation. After 24 h, cells were passed at low density (2000 cells/well) in 10 cm culture

dishes and selected with puromycin at 1.0 μg/ml for clonal expansion. The media was changed every 2 days until colonies were harvested using cloning cylinders.

2.4. Analysis of body weight, adiposity and food intake

To compile growth curves, mice were weighed once a week for 16 weeks, from weaning. Nuclear magnetic resonance (NMR, LF50, Bruker MiniSpec) was used to measure body composition (fat mass and lean mass) in mice. At the end of experiments, mice were sacrificed and various fat pads (interscapular brown, perirenal, gonadal, and inguinal fat pads), liver and kidneys were dissected and weighed. To measure food intake, mice were housed in individual cages. After 3 days of acclimation to individual housing, daily and cumulative food intake were measured over a 4-day period at 17 weeks of age.

2.5. Imaging of body fat and brain ventricles

Magnetic Resonance Imaging (MRI) of body fat and brain ventricles was performed after the animals were anesthetized (91 mg/kg ketamine and 9.1 mg/kg xylaxine, IP) using a Varian Unity/Inova 4.7 T small-bore MRI system (Varian Inc.). The acquisition consisted of a T1-weighted fast spin-echo sequence (repetition time/echo time = 625/12 ms) with an in-plane resolution of 0.13 × 0.25 mm^2 and a slice thickness of 5 mm acquired in the axial and coronal planes.

2.6. Glucose and insulin tolerance tests

Glucose tolerance tests were performed in overnight fasted mice. Blood samples were taken from the tail to measure blood glucose at baseline, and then mice were injected with glucose (2 mg/kg body weight, IP, Sigma—Aldrich). To test for the glucose-reducing effect of insulin, mice were fasted for 5 h. After baseline glucose levels were measured, mice were injected with insulin (0.5 unit/kg body weight, IP, Novo Nordisk). Blood glucose was measured at 15, 30, 60, and 120 min after injection of glucose or insulin. Blood glucose levels were determined using a glucometer (One Touch Ultra 1, LifeScan Inc.).

2.7. Mitochondria function assay by seahorse

For experiments in the Seahorse XF Analyzer, N39 and N39 Bbs1KO cells were plated onto 96-well Seahorse plates at a density of 20,000 per well 24 h before the experiment. The cells were equilibrated in Seahorse assay medium (unbuffered DMEM) for 1 h. Oligomycin, FCCP, and antimycin/rotenone were added to some wells at concentrations of 1, 1.5, and 2 μM respectively. All measurements were performed in triplicates. Cell numbers were automatedly count by Cytation5 from BioTek. Protein concentration was used to normalize oxygen consumption rate.

2.8. Mitochondrial purification

Mitochondria from N39 and N39-*Bbs1*KO cells were purified according to the method of Abcam Mitochondrial purification protocol for Western blot samples. The mitochondrial samples were used to detect DRP1 and BBS8 by Western blotting. GRP75 was used as internal control to normalize between two samples.

2.9. Mitochondrial morphometry by transmission electron microscopy (TEM)

Cells cultured to 95—100% confluence in cover glass (12 mm circle) in 24 wells were fixed with 2.5% glutaraldehyde (electron microscopy grade) and 2% paraformaldehyde in PBS. Cells were then washed with ice-cold 0.1 m sodium cacodylate 3 × 10 min on ice followed by postfixation in 1% osmium tetroxide, 0.8% potassium ferrocyanide in 0.1 m sodium cacodylate for 3 h on ice. After three washes in ice-cold ddH_2O for 10 min each, the tissue was stained in 2% uranyl acetate for 2 h. Slices were dehydrated in an ethanol series of ice-cold 20, 50, 70, and 90%, and then three washes in 100% ethanol at room temperature for 10 min each. Samples were infiltrated in 67% ethanol/33% Durcupan ACM (Fluka; Sigma—Aldrich) for 3 h at room temperature with agitation, then 33% ethanol/67% Durcupan ACM for 3 h at room temperature followed by 3 changes of 100% Durcupan for 8 h each at 22 °C with agitation. The Durcupan-infiltrated cells were then flat-mounted between two mold-release glass slides and polymerized at 60 °C for 2 days. Semithick sections were cut using a Leica EM UC7 ultramicrotome and placed on 50-mesh uncoated copper clamshell grids.

The specimens were irradiated for ∼30 min before initiating a tilt series to limit anisotropic specimen thinning during image collection. During data collection, the illumination was held to near parallel beam conditions. In each sample, several EM images were captured using Hitachi HT7800 randomly, all at the same magnification. The mitochondrial profile area, length and form factor (length/width) were measured using the ImageJFiji area and perimeter tools. To avoid bias, all the mitochondria in an image were measured. A total of at least three experiments were performed each time.

For tissue mitochondrial morphology analysis, mice anesthetized with ketamine and xylazine were transcardially perfused with PBS followed by 2% paraformaldehyde and 1.0% glutaraldehyde in PBS. Brown adipose tissue and brain were extracted from each mouse and post-fixed and then transferred to a preserving solution before sectioning. To identify POMC neurons, brain sections containing the arcuate nucleus of the hypothalamus were incubated with anti-POMC antibody (diluted 1:250 in 0.1M PB, Phoenix Pharmaceuticals; Cat# H-029-30). After several washes with PBS, sections were incubated with the secondary antibody (biotinylated goat anti-rabbit IgG; 1:250 in PBS; Vector Laboratories) for 2 h at room temperature, then rinsed in PBS three times 10 min each time and incubated for 2 h at room temperature with avidin—biotin—peroxidase (ABC; 1:250 in PB; ABC Elite kit, Vector Laboratories). The immunoreaction was visualized with 3,3-diaminobenzidine (DAB). Sections were then osmicated (1% osmium tetroxide) for 30 min, dehydrated through increasing ethanol concentrations (using 1% uranyl acetate in the 70% ethanol for 30 min), and flat-embedded in araldite between liquid release-coated slides (Electron Microscopy Sciences, Fort Washington, PA). After capsule embedding, blocks were trimmed. Ribbons of serial ultrathin sections were collected on Formvar-coated single slot grids and examined using a Hitachi HT7800 electron microscope. Mitochondrial profile area, length and form factor (length/width) were measured, as described above, in 3 mice/groups.

2.10. Confocal microscopy

Cells grown on coverslips precoated with 0.1% gelatin were transduced with adenovirus expressing mitochondrial targeted green fluorescent protein (mito-GFP, MOI 50) for 48 h, fixed in 4% paraformaldehyde and then mounted in VECTASHIELD mounting medium with 4′,6-diamidino-2-phenylindole (DAPI). Images were acquired using a Zeiss LAM 880 confocal microscope. For morphometry analysis, images were processed using NIH ImageJ software with the plugins involving either "rolling ball" background subtraction or deblurring by 2-D deconvolution with a computed point spread function. Using a custom-written NIH ImageJ macro we developed, processed images were converted to binary (black and white) images by auto thresholding, and mitochondrial particles were analyzed for length or form factor (perimeter 2/(4 × π × area). The parameters for form factor are set with minimum value of 1 for perfectly circular mitochondria.

To analyze mitochondria distribution, cells growing on "Y"-shaped micropatterned substrates (purchased from CYTOO company) were selected based on shape (visualized with phalloidin) and nuclei (visualized with DAPI) to ensure that only single cells properly attached to the micropatterns were used. The mitochondrial area was thresholded, and Sholl analysis of mitochondrial distribution was performed using a custom-made ImageJ plugin [29]. Mitochondrial signal was quantified within shells radiating out from the soma at 1 μm intervals and the cumulative distribution of mitochondrial signal or Mitochondrial Probability Map (MPM) was plotted per genotype.

2.11. Scanning electron microscopy

Mice anesthetized with ketamine and xylazine were transcardially perfused with 0.9% saline followed by fixative solution (4% paraformaldehyde, 15% picric acid, 0.1% glutaraldehyde in 0.1 M PBS). The lateral wall of the lateral ventricles dissected from mouse brains were dehydrated in ethanol and dried by using a critical point drier. The samples were then mounted on an aluminum stub using double-stick carbon tape, coated with gold/palladium by using a sputter coater. Ependymal cilia were imaged using a Hitachi S-4800 scanning electron microscope (Hitachi, Pleasanton, California).

2.12. Immunofluorescence

Mice anesthetized with ketamine and xylazine were perfused with PBS (5 ml/min; 15 ml) followed by 4% paraformaldehyde/HistoChoice Tissue Fixative (Amresco) in PBS (3 ml/min; 45 ml) using Harvard PHD 22/2000 Syringe Pump. Entire brain was excised and incubated in the same fixative overnight at 4 °C. Fixed brains were washed 3 times with PBS and incubated in 30% sucrose/PBS overnight with one change of solution after 4–6 h of initial incubation. Brains were vibratome-sectioned with 30 μm thickness. Immunochemistry was performed on brain sections to detect phosphorylated signal transducer and activator of transcription 3 (STAT3) as described previously [21] by using a 1:250 dilution of a rabbit polyclonal anti-phospho-STAT3 antibody. Processed brain sections were mounted using VectaShield® mounting medium with DAPI. Images were visualized using confocal microscopy (Zeiss LSM710) and analyzed as CFCT using ImageJ software.

2.13. Measurement of intracellular and mitochondrial Ca^{2+}

To measure mitochondria Ca^{2+}, N39 and N39-*Bbs1*KO cells were transiently transfected with mtRGRC plasmid for 48 h before incubation with 2 μM Fura 2 acetoxymethyl ester with 0.01% pluronic acid in a HEPES-buffered Hank's salt solution (HH buffer: 140 mM NaCl, 5 mM KCl, 1.3 mM CaCl2, 1 mM MgCl2, 10 mM HEPES, 10 mM glucose, pH 7.4 with KOH (310 mOsm/kg with sucrose) for 30 min to perform the cytosol ($[Ca^{2+}]i$), and used to measure intracellular Ca^{2+} in response to Platelet Derived Growth Factor-BB (PDGF-BB, 20 ng/ml).

Simultaneous monitoring of the Ca^{2+} concentrations in the cytosol ($[Ca^{2+}]$cyt) and mitochondria ($[Ca^{2+}]$mt) of cultured cells was performed as previously described [30]. Cells were placed in a flow-through perfusion chamber and mounted on an inverted IX-71 Olympus microscope (Olympus). Cells were perfused with a HH buffer. $[Ca^{2+}]$cyt and $[Ca^{2+}]$mt elevations in the cells were stimulated with PDGF-BB and then elicited by brief (15 s) depolarization using 30 mM KCl.

Fura-2 and mito-RGECO1 were sequentially excited at 340 nm (12 nm bandpass), 380 nm (12 nm bandpass), and 550 nm (12 nm bandpass) using a Polychrome V monochromator (TILL Photonics, Germany) and a 40× oil-immersion objective (NA = 1.35, Olympus). Excitation/emission fluorescence was separated using a dual fluorophore beamsplitter (FF493/574-Di01, Semrock) while signal was collected using a dual emission filter (FF01-512/630, Sem-rock) and an IMAGO CCD camera (640 × 480 pixels; Till Photonics). Fluorescent images were acquired at a rate of 0.5 Hz. The changes in $[Ca^{2+}]$cyt were quantified as Fura-2 fluorescence ratio (R = 340/380 nm). Changes in $[Ca^{2+}]$mt were quantified as $\Delta F/F_0 = (F-F_0)/F_0$, where F is current fluorescence intensity (λex = 550 nm) and F_0 is the fluorescence intensity at baseline. At each wavelength, fluorescence was corrected for background as measured in an area free of cells.

2.14. Electroretinography (ERG)

Mice were dark adapted overnight. Under red light, mice were anesthetized by IP injection of ketamine (17.5 mg/cc)/xylazine (2.5 mg/cc) (100 μL/20 g body weight). After anesthesia, the eye was dilated for 5 min through application of phenylephrine HCl (Paragon). Recordings (10 sweeps per intensity, 1 ms per sweep, green light) were made at 0.019, 0.1564, 1.252, and 40 cd s/m^2 using the ERG system (Phoenix Research Labs) and LabScribe2 ERG software. After recordings, animals were allowed to recover on a heat pad.

2.15. Retinal histology

Mice were anesthetized with IP ketamine and xylazine mixture (200 μL/20 g body weight), and transcardial perfusion was performed using PBS followed by 10% formalin (approximately 4% formaldehyde). Eyes were enucleated, and a small puncture was created through the lens using a 26G syringe. Eyes were then embedded in Tissue-Tek O.C.T. compound and frozen in a 2-methybutane bath chilled with liquid nitrogen. Eyes were sectioned using a Cryostat microtome at thickness of 10 μm and stored at −80 °C until further use. Sections were processed with hematoxylin and eosin histology and visualized under a light microscope at 40× magnification. Retinal images inferior to the optic nerve were acquired. Four images per animal were randomly selected and thicknesses of retinal layers were quantified in these four images using ImageJ. Imaging and quantification of the retinas were performed while masked to the genotypes of the samples. Thicknesses of retinal layers from these four images were averaged to yield the measurements for one animal. For adipose tissue and testis, sections were processed with hematoxylin and eosin histology and visualized under a light microscope at 20× or 40× magnification. For adipocyte area analysis, BZ-X800 Analyzer software from Keyence was used.

2.16. Sucrose gradient fractionation

Sucrose gradient assay was performed as previously described [31]. Briefly, protein lysates were centrifuged at 20,000×*g* for 20 min. The supernatants were loaded onto a 20–60% sucrose gradient. The gradient was centrifuged at 100,000×*g* for 14 h using a TH-660 rotor Thermo Scientific (Asheville, NC). Two hundred-microliter fractions were taken from the top and precipitated by cold acetone. Precipitated samples were spun at 20,000×*g* for 15 min. The pellets were dissolved in SDS-PAGE sample buffer and used for Western blotting.

2.17. Co-immunoprecipitation assay

Testes obtained from mice, after sacrifice, were lysed with lysate buffer (50 mM HEPES, pH 7.5, 150 mM NaCl, 1 mM $MgCl_2$, 1 mM $CaCl_2$, 10 mM NaF, 5 mM EDTA, 1% Triton, 2 mM sodium orthovanadate and Roche cocktail protease inhibitor tablet). Protein samples (800 μg) were subjected to immunoprecipitation assay with 5 μg anti-BBS5 antibody (Proteintech, Cat#: 14569-I-AP) or normal rabbit IgG. Immunocomplex was separated on a 9% SDS-PAGE gel, transferred to PVDF membrane, then probed with anti-DRP1 antibody (BDTransduction Laboratories, Cat.# 611113, 1:1000) or BBS5 antibody from Santa Cruz (Cat.# sc-515331, 1:1000), followed by a goat anti-mouse

HRP (Cell Signaling, 7076, 1:10000). Protein expression was visualized with ECL detection kit (GE healthcare).

2.18. Western blot analysis

Proteins were extracted by homogenizing the cells or tissue in tissue lysate buffer (50 mM HEPES, pH 7.5, 150 mM NaCl, 1 mM MgCl2, 1 mM CaCl2, 10 mM NaF, 5 mM EDTA, 1% Triton, 2 mM sodium orthovanadate and Roche cocktail protease inhibitor tablet). Twenty μg protein samples were subjected to SDS PAGE, electrotransferred on a polyvinylidene fluoride membrane, then probed with primary antibodies (1:1000) targeting the following proteins: DRP1, pDRP1(Ser616), pDR1(Ser637), MCU, OPA1, MFF, BBS8 and AKAP1. Total OXPHOS rodent WB antibody cocktail followed by a secondary anti-rabbit antibody (1:10,000) to determine mitochondrial Complex I—V. Protein expression was visualized with ECL detection kit (GE healthcare).

2.19. Data analysis

The data are expressed as means ± SEM. Data were analyzed using *t*test, 1 way- or repeated measures 2-way ANOVA. When ANOVA reached significance, a post-hoc comparison was made using Bonferroni's test, Fisher test or Tukey's test. GraphPad PRISM 9.1.0 was used for statistical analysis. A $P < 0.05$ value was considered to be statistically significant.

3. RESULTS

3.1. BBSome deficiency affect mitochondria morphology

We used the CRISPR/Cas9 technology with a guide RNA targeting exon 4 of *Bbs1* gene to generate a stable mouse knockout hypothalamic N39 neuronal cell line (*Bbs1*KO). We confirmed *Bbs1* gene deletion by DNA sequencing. To verify BBSome deficiency in these cells, we tested the trafficking of endogenous BBS proteins in cilia. The ciliary localization of endogenous BBS2 and BBS9 was impaired in *Bbs1*KO cells relative to wild type control cells (Supplemental Figure S1A-B). Notably, analysis of mitochondrial morphology with TEM revealed that BBSome deficient cells exhibit elongated mitochondria (Figure 1A). This was confirmed by measuring the area, form factor and length of mitochondrial profiles (Figure 1A—D). We further examined mitochondrial

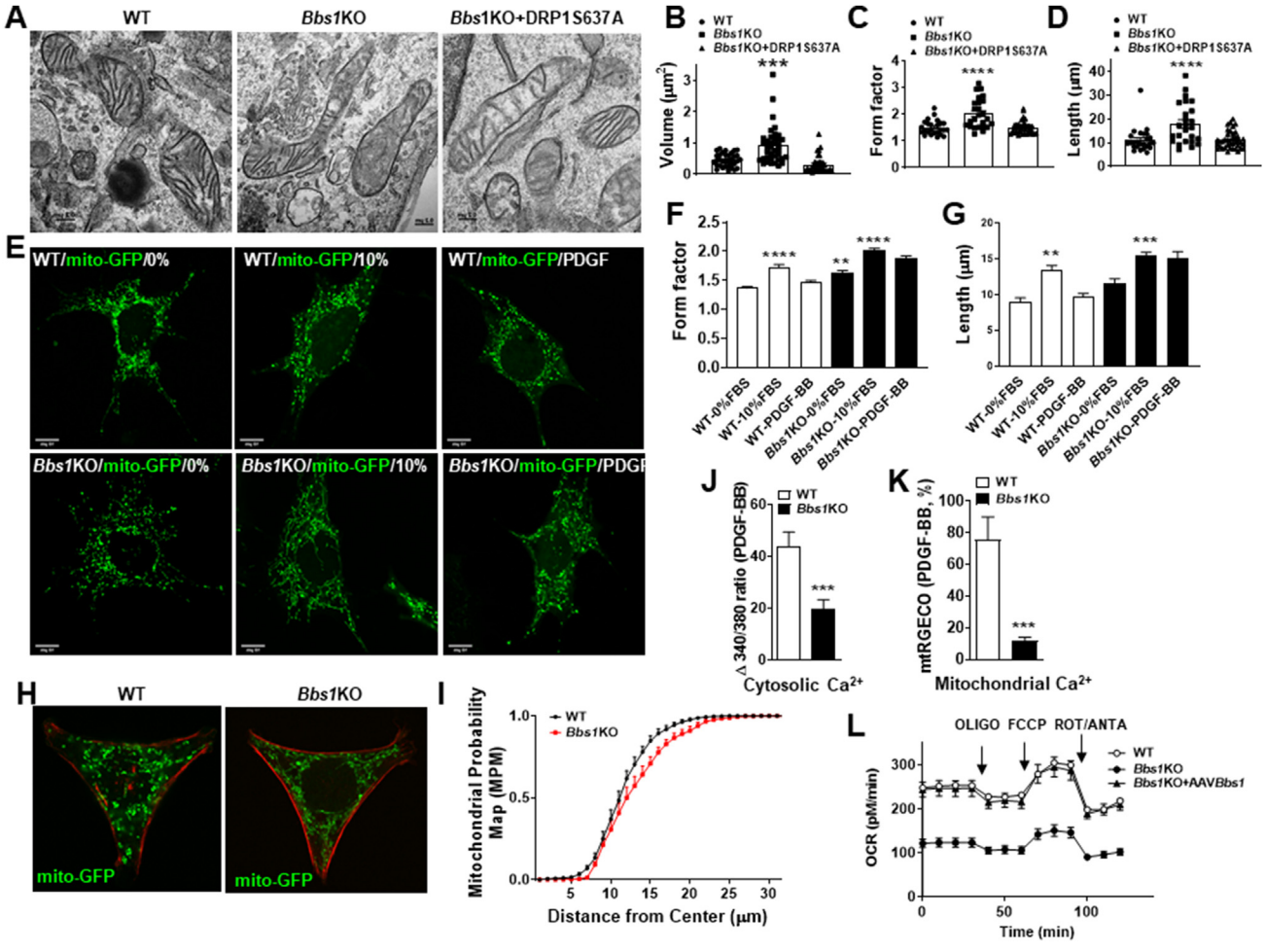

Figure 1: Mouse hypothalamic cells lacking the *Bbs1* gene display elongated mitochondria. (A—D) Representative TEM images of mitochondria (A) and related quantification of mitochondrial area (B), form factor (C) and length (D) in N39 (WT) and N39-*Bbs1*KO (*Bbs1*KO) with or without FIV-DRP1S637A (n = 3, 16 images/group). (E—G) Representative images of mitochondria (E) and related quantification of the form factor (F) and mitochondria length (G) in cells infected with mito-GFP then serum starved or cultured with 10%FBS with or without PDGF-BB overnight (n = 3, 30 images/group). (H—I) Representative images of mito-chip assay (I) and related quantification of mitochondria distribution (J) in WT and *Bbs1*KO cells (n = 3, 16 images/group). (J—K) Cytosolic (J) and mitochondrial (K) Ca^{2+} induced by PDGF-BB in WT and *Bbs1*KO cells (n = 3, 24 cells/group). (L) Comparison of oxygen consumption rate (OCR) between WT and *Bbs1*KO cells (n = 7/group). OLIGO: Oligomycin, FCCP: Carbonyl cyanide 4-(trifluoromethoxy) phenylhydrazone, ROT/ANTA: Rotenone/Antimycin A. Data are mean ± SEM and were analyzed by one-way ANOVA except for L, analyzed with repeated measures (RM) two-way ANOVA, and J-K, analyzed by *t*test. $^{**}P < 0.01$, $^{***}P < 0.001$ and $^{****}P < 0.0001$ vs. WT (and vs *Bbs1*KO + DRP1S637A in B—C).

morphology using mitochondrial targeted GFP (mito-GFP) that enables detection and quantification by fluorescence microscopy [32]. We used this approach to assess whether loss of the *Bbs1* gene affect mitochondria response to stimuli such as metabolic challenge [33] and PDGF-BB [34,35]. Consistent with the TEM data, form factor and length of mitochondria were higher in *Bbs1*KO cells relative to control cells in three different conditions: serum starvation (12 h), with 10% FBS or 10% FBS plus 20 ng/ml PDGF-BB for 12 h (Figure 1E—G). This indicates that a functional BBSome is required for proper mitochondria morphology and fission/fusion equilibrium.

To test whether disruption of the BBSome causes similar changes in other cell types, we studied mitochondrial shape in IMCD3-*Bbs1*KO cells, an inner medullary collecting duct cell line, generated using the CRISPR/Cas9 system [22]. Using mito-GFP labeling, we observed that form factor and mitochondrial length were significantly higher in IMCD3-*Bbs1*KO compared to control cells (Supplemental Figure S2A-C). TEM analysis confirmed the morphological changes in the mitochondria of IMCD3-*Bbs1*KO cells, including significant increase in mitochondrial area, form factor and length (Supplemental Figure S2D-G). Of note, abnormalities in mitochondria morphology were also observed in fibroblast cells derived from human patients harboring a homozygous M390R missense mutation in the *BBS1* gene (Supplemental Figure S2H). Together, these data demonstrate morphological alterations in mitochondria as a common consequence of BBSome deficiency.

3.2. BBSome deficiency compromises mitochondrial function

To test the implications of the morphological changes in mitochondria induced by loss of the BBSome, we assessed mitochondrial function. Correct mitochondrial position within cells plays an important role in cell division, migration, and survival [36]. Actin- and microtubulin-dependent mitochondrial trafficking are two major mechanisms that mediate mitochondrial mobility. Thus, we examined mitochondrial distribution using a CYTOOchips™ micropattern assay. We found that mitochondrial distribution was shifted away from the nucleus (a right shift in the graph) in *Bbs1*KO cells compared to control cells (Figure 1H—I). Since mitochondrial function is closely tied to intracellular Ca^{2+} signaling, we examined the effect of *Bbs1* gene deletion on Ca^{2+} transients evoked by PDGF-BB [34]. Interestingly, PDGF-BB-induced cytosolic and mitochondrial Ca^{2+} transients were significantly diminished in *Bbs*1KO cells compared to the control cells (Figure 1J—K and Supplemental Figure S1C-D). Finally, cell mitochondria stress test revealed a significantly lower oxygen consumption rate in *Bbs1*KO cells compared to control cells, indicating mitochondrial respiratory dysfunction (Figure 1L). Notably, re-expression of the *Bbs1* gene rescued the decrease in oxygen consumption rate in *Bbs1*KO cells indicating that the mitochondria defects are due to the loss of this gene. Together, these data demonstrate that the morphological changes in the mitochondria evoked by loss of the BBSome translate into functional abnormalities.

3.3. BBSome-mediated control of mitochondria involves DRP1

Next, we investigated the mechanisms underlying BBSome regulation of mitochondria by focusing on proteins that mediate fusion and fission. Expression of OPA1 that mediate fusion was not different in *Bbs1*KO cells relative to control cells (Supplemental Figure S1E-F). On the other hand, the level of DRP1 protein that regulate mitochondrial fission was significantly decreased in *Bbs1*KO cells compared to WT cells (Figure 2A—B). We next examined the status of DRP1 phosphorylation sites Ser616 and Ser637, which determines its activity [6,13]. Notably, DRP1 phosphorylation at Ser616 (pDRP1(Ser616) was significantly decreased in *Bbs1*KO cells compared to control cells (Figure 2A,C and Supplemental Figure S2I-K). Importantly, the decreased level of pDRP1(Ser616) was mostly rescued by re-expression of the *Bbs1* gene in *Bbs1*KO cells (Figure 2A,C) linking the low pDRP1(Ser616) level to *Bbs1* gene deletion. A decrease in pDRP1(Ser616) is expected to reduce fission [13], which is consistent with the elongated mitochondria in *Bbs1*KO cells.

DRP1 phosphorylation at Ser637 by PKA is known to promote mitochondrial fusion by inhibiting DRP1 activity. Since we were unable to detect pDRP1 (Ser637) under basal conditions, we determined the effect of BBSome loss on Ser637 phosphorylation following PKA activation. As expected, forskolin treatment caused a significant increase in pDRP(Ser637) in control cells that was associated with a decrease in pDRP1(Ser616) (Figure 2D—F). Interestingly, these responses were blunted in *Bbs1*KO cells. Moreover, infecting N39-*Bbs1*KO or IMCD3-*Bbs1*KO cells with a DRP1S637A mutant, a mimetic of the dephosphorylated state [13,25], rescued the decrease in pDRP1(Ser616) phosphorylation (Figure 2G—H and Supplemental Figure S2I-K) and reversed the changes in mitochondrial morphology (Figure 1A—D and Figure 2I—K). These findings point to dysregulation of DRP1 phosphorylation as the main cause of the morphological and functional changes in mitochondria evoked by BBSome deficiency.

3.4. The BBSome interacts with mitochondria

To further understand how the BBSome regulate DRP1, we considered the possibility that the BBSome and DRP1 may interact physically. However, using a co-immunoprecipitation assay we failed to detect an interaction between the BBSome and DRP1 (Supplemental Figure S3). The BBSome was previously found to interact with clathrin heavy chain (CHC) [37], which in turn interact with DRP1 [38,39]. Our attempts to use a co-immunoprecipitation assay to confirm the interaction between the BBSome and CHC failed as both the BBSome and CHC do not specifically bind to protein A/G beads (data not shown). Next, we used sucrose gradient fractionation that separates protein and protein complexes based on their molecular weight to assess whether the BBSome is present in the same fraction as CHC and DRP1. We identified a partial localization of the BBSome and CHC, (sample fraction between 9 and 16) and of DRP1 and CHC (sample fraction between 6 and 11, Figure 3A). This finding raises the possibility that CHC may mediate the interaction between the BBSome and DRP1. Interestingly, we observed a partial co-localization of BBS3 with MFN2 in sucrose gradient fractions 4 to 9 (Figure 3A), pointing to the possibility that the BBSome interaction with mitochondria may also involve BBS3 and MFN2.

We also tested the possibility that the BBSome may interact directly with mitochondria. To test this, we transfected WT and *Bbs1*KO cells with a BBSome protein (BBS7) tagged with a red fluorescent protein. We observed strong colocalization of BBS7 and mitochondria marker (mito-GFP) in WT cells (Figure 3B). However, the mitochondrial localization of the BBSome was absent in *Bbs1*KO cells. We also detected another BBSome protein (BBS8) from purified mitochondria (Figure 3C), which was significantly reduced in *Bbs1*KO cells (Figure 3C—D). Additionally, DRP1 protein was significantly decreased in mitochondria isolated from *Bbs1*KO cells (Figure 3C,E), suggesting that absence of the BBSome disrupts DRP1 targeting to the mitochondria.

3.5. BBSome deficient mice display mitochondrial abnormalities

To test whether the mitochondria abnormalities observed in cultured cells occur *in vivo*, we assessed mitochondria in POMC neurons and brown adipose tissue of mice lacking the BBSome specifically in POMC

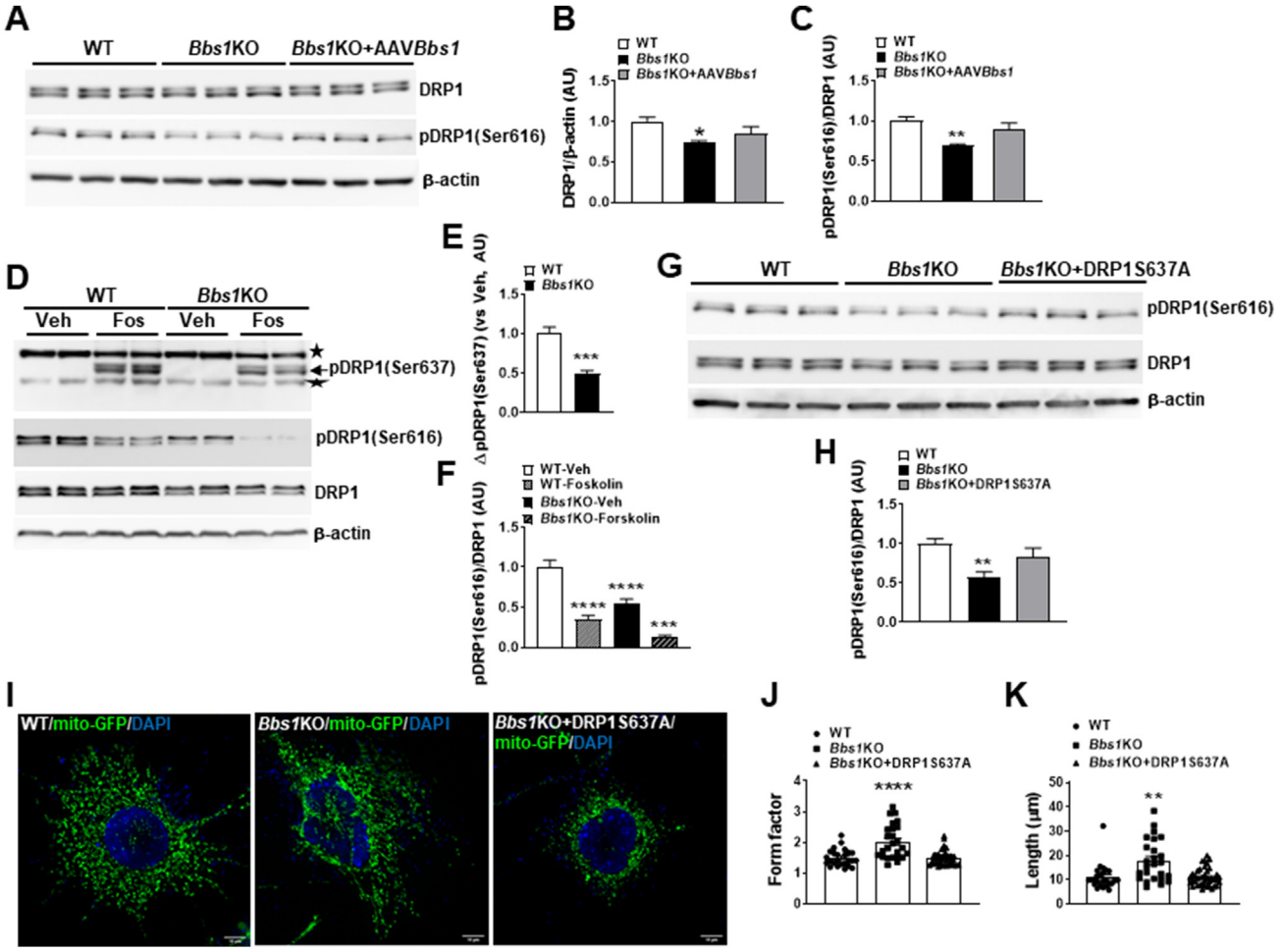

Figure 2: Role of DRP1 in mitochondria defects evoked by BBSome deficiency. (A–C) Representative Western blots (A) and related quantification of DRP1 (B) and pDRP1(Ser616) (C) in N39 (WT), N39-*Bbs1*KO (*Bbs1*KO) and N39-*Bbs1*KO infected with AAV-*Bbs1* (n = 9/group). (D–F) Representative Western blots (D) and related quantification depicting the effect of PKA activator, forskolin (25 μM, 1h), on pDRP1(Ser637) (E) and pDRP1(Ser616) (F) in WT and *Bbs1*KO cells (n = 9/group). (G–H) Representative Western blots (G) and related quantification (H) of pDRP1(Ser616) in WT and *Bbs1*KO cells with or without FlV-DRP1S637A (n = 9/group). (I–K) Representative mitochondria (mito-GFP) images (I) and related quantification of the form factor (J) and mitochondria length (K) in WT and *Bbs1*KO cells with or without FlV-DRP1S637A (n = 3, 30 images/group). Data are mean ± SEM and were analyzed by one-way ANOVA except data in E analyzed by *t*test. **P < 0.01, ***P < 0.001, ****P < 0.0001 vs WT group.

neurons (POMC^{Cre}/*Bbs1*$^{fl/fl}$ mice) and adipocytes (Adipo^{Cre}/*Bbs1*$^{fl/fl}$ mice), respectively. Interestingly, we observed the expected morphological changes in mitochondria of POMC neurons of POMC^{Cre}/*Bbs1*$^{fl/fl}$ mice (Figure 4A) and brown adipose tissue of Adipo^{Cre}/*Bbs1*$^{fl/fl}$ mice (Figure 4E) compared to their control littermates. Specifically, mitochondrial area, form factor and length were significantly higher in POMC neurons of POMC^{Cre}/*Bbs1*$^{fl/fl}$ mice (Figure 4B–D). Mitochondrial form factor and length were also significantly higher in brown adipocytes of Adipo^{Cre}/*Bbs1*$^{fl/fl}$ mice relative to control littermates (Figure 4F–H). These results indicate that the morphological changes in mitochondria evoked by BBSome disruption are recapitulated *in vivo*. Next, we examined levels of DRP1 and active pDRP1(Ser616) in the hypothalamus of global BBS null mice. Interestingly, the pDRP1(Ser616) level was significantly decreased in the hypothalamus of *Bbs8*$^{-/-}$ and *Bbs4*$^{-/-}$ mice (Figure 4I,K and Supplemental Figure S4A-B). As in cells, pDRP1(Ser637) was not detectable in mouse hypothalamic samples by Western blot. No significant change in total DRP1 protein expression was noted in the hypothalamus of *Bbs8*$^{-/-}$ or *Bbs4*$^{-/-}$ mice (Figure 4I–J and Supplemental Figure S4A and C). There was also no difference in the hypothalamic levels of mitochondrial calcium uniporter (MCU), MFN2, OPA1 and MFF in BBS mice, whereas a decrease in hypothalamic mitochondrial complex I and III, but not complex II, IV and V, was noted only in *Bbs8* null mice (Supplemental Figure S4A-X). These changes in mitochondrial proteins, particularly the reduced pDRP1(Ser616), point to inhibition of mitochondrial fission in the hypothalamus of BBS mice.

3.6. *Akap1* heterozygosity rescues the mitochondria defects evoked by BBSome deficiency

To understand the physiological significance of the mitochondrial alterations evoked by BBSome deficiency, we asked whether restoring mitochondrial fission/fusion process will correct the phenotypes caused by loss of the BBSome. Based on our findings that the expression of DRP1S637A normalized pDRP1(Ser616) level and rescues mitochondrial morphology, we reasoned that preventing DRP1 phosphorylation at Ser637 would rescue the decreased pDRP1(Ser616) and alleviate the phenotypes induced by BBSome deficiency. For this, we targeted AKAP1 that increases mitochondrial length by promoting the phosphorylation of DRP1(Ser637) [15,40]. We generated mice that carry one copy of the *Akap1* gene on a *Bbs8* null background (*Akap1*$^{+/-}$/*Bbs8*$^{-/}$

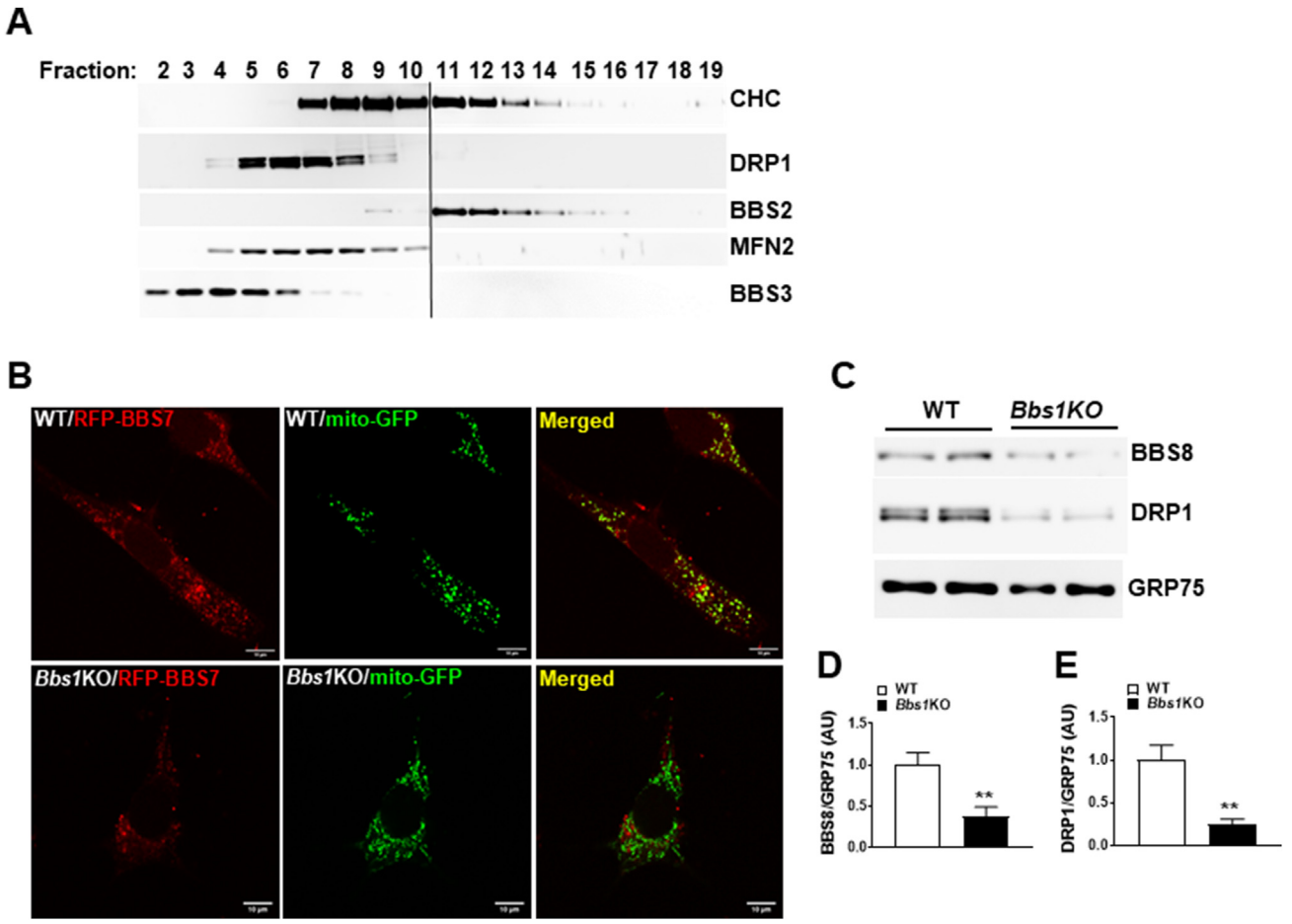

Figure 3: Interaction between the BBSome and mitochondria. (A) Representative Western blots of sucrose gradient showing partial co-localization of the endogenous CHC and DRP1 (fraction 7–9), CHC and BBS2 (fraction between 9 and 16) and BBS3 and MFN2 (fraction between 4 and 8) in human RPE1 cells (n = 3). (B) Representative images of co-localization of red fluorescent protein (RFP)-tagged BBS7 with mitochondria in N39 (WT) cells, but not in N39-*Bbs1*KO (*Bbs1*KO) cells (n = 3). (C–E) Representative Western blots (C) and related quantification (D–E) of BBS8, DRP1 and GRP75 (loading control) in purified mitochondria from WT and *Bbs1*KO cells (n = 8/group). Data are mean ± SEM and were analyzed by *t*test. **P < 0.01 vs WT group.

$^{-}$). As expected, BBS8 protein was detected in the hypothalamus of control mice (*Akap1*$^{+/+}$/*Bbs8*$^{+/+}$) but not in *Akap1*$^{+/+}$/*Bbs8*$^{-/-}$ or *Akap1*$^{+/-}$/*Bbs8*$^{-/-}$ mice (Supplemental Figure S5). AKAP1 protein expression was reduced by about 50% in *Akap1*$^{+/-}$/*Bbs8*$^{-/-}$ mice relative to *Akap1*$^{+/+}$/*Bbs8*$^{-/-}$ mice and control littermates. Importantly, the decrease in the hypothalamic pDRP1(Ser616) level induced by loss of the BBSome was rescued by *Akap1* heterozygosity without affecting the total DRP1 level (Figure 5A–C). This was associated with correction of the profile area, form factor and length of mitochondria of hypothalamic neurons (Figure 5D–G).

3.7. Mitochondrial involvement in the sperm flagella defect, but not male infertility and photoreceptor degeneration induced by BBSome deficiency

Absence of the BBSome is known to cause specific abnormalities in the sperm flagella leading to infertility [41,42]. We tested whether these abnormalities can be reversed by rescuing the mitochondria defects. Although male *Akap1*$^{+/-}$/*Bbs8*$^{-/-}$, but not *Akap1*$^{+/+}$/*Bbs8*$^{-/-}$, mice showed sperm flagella at 8–10 weeks of age, the sperm flagella were lost at 20 weeks of age (Supplemental Figure S6A). The testis of male *Akap1*$^{+/+}$/*Bbs8*$^{-/-}$ mice were significantly smaller compared to controls (Supplemental Figure S6B). This was slightly improved in *Akap1*$^{+/-}$/*Bbs8*$^{-/-}$ mice. Next, we tested whether male *Akap1*$^{+/-}$/*Bbs8*$^{-/-}$ mice are fertile. However, breeding of three *Akap1*$^{+/-}$/*Bbs8*$^{-/-}$ male mice (8 weeks old) with control female mice for 3 months failed to produce any pups, indicating that *Akap1* heterozygosity does not rescue male *Bbs8*$^{-/-}$ infertility.

To test whether *Akap1*$^{+/-}$/*Bbs8*$^{-/-}$ mice rescue photoreceptor degeneration, a common phenotype of BBSome deficiency, we performed an electroretinogram (ERG) and histological analysis. However, rescuing the mitochondria defects did not appear to improve this phenotype as we did not find significant differences in either ERG at 0.019, 0.16, 1.25 and 40 cd s/m^2 a- or b-wave (Supplemental Figure S6C-D) nor in histology of outer and inner nuclear layer thickness (Supplemental Figure S6E-F) between 5 months old *Akap1*$^{+/-}$/*Bbs8*$^{-/-}$ and *Akap1*$^{+/+}$/*Bbs8*$^{-/-}$ mice. Surprisingly, we found that the inner nuclear layer thickness was significantly reduced in *Akap1*$^{+/+}$/*Bbs8*$^{-/-}$ mice compared to control littermates (Supplemental Figure S6E and G), a phenotype that was not reported previously. This phenotype was not rescued in *Akap1*$^{+/-}$/*Bbs8*$^{-/-}$ mice confirming that the photoreceptor degeneration associated with BBS does not involve mitochondria.

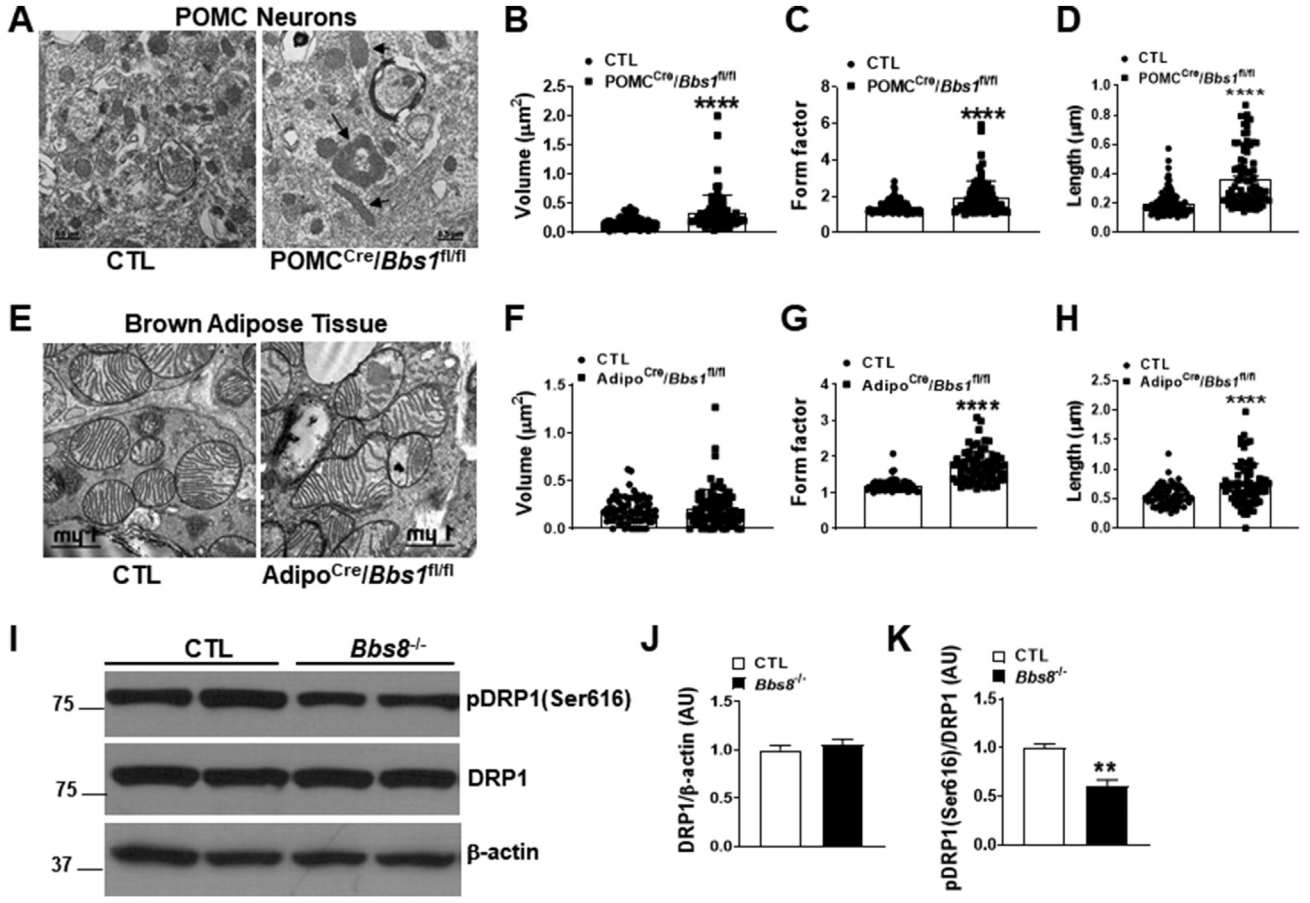

Figure 4: BBSome deficiency affect mitochondria dynamics *in vivo*. (A–D) Representative TEM images of mitochondria (A) and related quantification of mitochondrial volume (B), form factor (C) and length (D) in POMC neurons of control (CTL) and POMC^{Cre}/*Bbs1*$^{fl/fl}$ mice. Arrows indicate defective mitochondria (n = 3, 12 images/group). (E–H) Representative mitochondrial TEM images (E) and related quantification of the mitochondrial area (F), form factor (G) and length (H) in brown adipocytes of CTL and Adipo^{Cre}/*Bbs1*$^{fl/fl}$ mice (n = 3, 12 images/group). (I–K) Representative Western blots (I) and quantitation of DRP1 (J) and pDRP1 (ser616) (K) in the hypothalamus of CTL and *Bbs8*$^{-/-}$ mice, (n = 4/group). Data are mean ± SEM and were analyzed by *t*test. **P < 0.01 and ****P < 0.0001 vs CTL.

3.8. *Akap1* heterozygosity ameliorates the neuroanatomical abnormalities associated with BBSome deficiency

Enlargement of the brain ventricles (hydrocephalus) is a common phenotype of BBS [43]. Thus, we assessed the contribution of mitochondria abnormalities to this phenotype. Magnetic Resonance Imaging was used to scan and determine the volume of the brain ventricles and further validated in neutral red-stained coronal brain sections. The ventricular enlargement caused by *Bbs8* gene deletion was reduced by about 50% by *Akap1* heterozygosity (Figure 6A–C). Next, we used transmission electronic scanning microscopy to assess ependymal cilia, which play an important role in the production and flow of cerebrospinal fluid. *Akap1*$^{+/+}$/*Bbs8*$^{-/-}$ mice displayed alterations in the ultrastructure and number of motile cilia of the ependymal cells lining the lateral ventricles while *Akap1* heterozygosity reversed these alterations to near normal (Figure 6D). Transmission electron microscopy analysis confirm the ciliary aberrations (shorter cilia with swollen distal region) in the *Akap1*$^{+/+}$/*Bbs8*$^{-/-}$ mice (Figure 6E). These abnormalities were partially corrected in *Akap1*$^{+/-}$/*Bbs8*$^{-/-}$ mice. Moreover, transverse sections showed loss of the 9 + 2 axonemal arrangements of microtubules in *Akap1*$^{+/+}$/*Bbs8*$^{-/-}$ mice which was restored in *Akap1*$^{+/-}$/*Bbs8*$^{-/-}$ mice (Figure 6F). These findings show the contribution of the mitochondria defects to the neuroanatomical phenotype induced by BBSome deficiency.

3.9. Mitochondria defects contribute to the metabolic alterations evoked by BBSome deficiency

BBSome deficiency leads to obesity in human and animal models [44]. Thus, we assessed whether AKAP1 deficiency-mediated normalization of mitochondrial function rescues the obesity phenotype in *Bbs8*$^{-/-}$ mice. Of note, there was no difference in body weight between littermate control mice (*Akap1*$^{+/+}$/*Bbs8*$^{+/+}$) and mice carrying at least one allele of the *Bbs8* gene (*Akap1*$^{+/-}$/*Bbs8*$^{+/+}$, *Akap1*$^{+/+}$/*Bbs8*$^{+/-}$ and *Akap1*$^{+/-}$/*Bbs8*$^{+/-}$ mice; Supplemental Figure S7A-B). Similar to other BBS mice [42,43], both male and female *Akap1*$^{+/+}$/*Bbs8*$^{-/-}$ were smaller at weaning than their littermate controls, but at 8–9 weeks of age they had similar body weight than control mice and then Akap1$^{+/+}$Bbs8$^{-/-}$ start gaining more weight (Figure 7A–B). At 16 weeks of age, *Akap1*$^{+/+}$/*Bbs8*$^{-/-}$ mice exhibited higher body weight, fat mass and liver mass whereas lean mass was lower, with statistical significance reached in males only (Figure 7A–E and Supplemental Figure S7C-F). Similar to *Akap1*$^{+/+}$/*Bbs8*$^{-/-}$ mice, *Akap1*$^{+/-}$/*Bbs8*$^{-/-}$ mice were also smaller at weaning, indicating that this phenotype is not rescued by *Akap1* heterozygosity. On the other hand, male *Akap1*$^{+/-}$/*Bbs8*$^{-/-}$ mice gained significantly less weight, adiposity and liver mass relative to *Akap1*$^{+/+}$/*Bbs8*$^{-/-}$ mice (Figure 7A,C and Supplemental Figure S7E-F). Consistent with these findings, the increase in adipocyte size evoked by loss of the BBSome

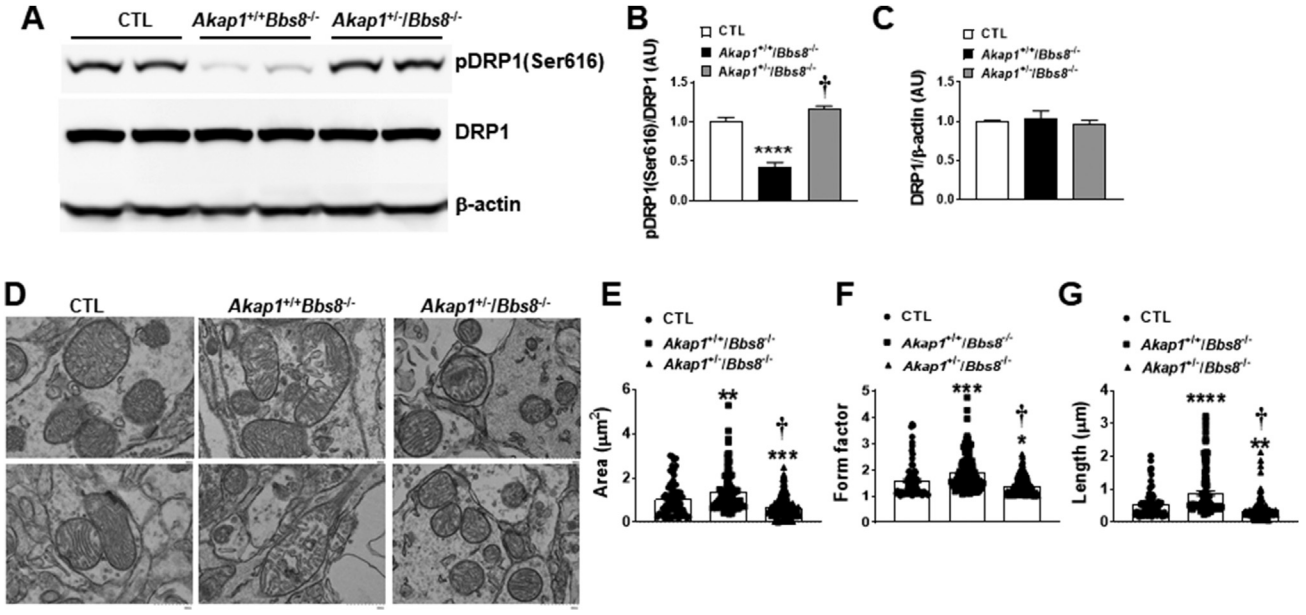

Figure 5: *Akap1* heterozygosity rescues mitochondria defects in BBSome deficient mice. (A–C) Representative Western blots (A) and quantitation of DRP1(Ser616) (B) and DRP1 (C) in the hypothalamus of control (CTL), $Akap1^{+/+}/Bbs8^{-/-}$ and $Akap1^{+/-}/Bbs8^{-/-}$ mice (n = 6/group). (D–G) Representative TEM images of mitochondria (D) and quantitation of mitochondrial volume (E), form factor (F) and length (G) in in the hypothalamus of control (CTL), $Akap1^{+/-}/Bbs8^{-/-}$ and $Akap1^{+/-}/Bbs8^{-/-}$ mice (n = 3, 16 images/group). Data are mean ± SEM and were analyzed by one-way ANOVA. *P < 0.05, **P < 0.01, ***P < 0.001, and ****P < 0.001 vs CTL; †P < 0.0001 vs $Akap1^{+/+}/Bbs8^{-/-}$ mice.

was blunted in $Akap1^{+/-}/Bbs8^{-/-}$ mice (Figure 7F–G). These protective effects were less pronounced in female $Akap1^{+/-}/Bbs8^{-/-}$ mice (Figure 7B,D, and Supplemental Figure S7F). The hyperphagia associated with BBSome deficiency was also attenuated by Akap1 heterozygosity with a more pronounced effect in males (Figure 7H–I). These findings implicate mitochondria dysfunction in the development of obesity and hyperphagia in BBS.

Next, we performed glucose and insulin tolerance tests to determine whether rescuing the mitochondria defects reverses the abnormalities in glucose metabolism and insulin sensitivity induced by loss of the BBSome. As expected, both male and female $Akap1^{+/+}/Bbs8^{-/-}$ mice displayed glucose intolerance (Figure 7J–M). This abnormality was improved in $Akap1^{+/-}/Bbs8^{-/-}$ mice particularly in males. $Akap1^{+/+}/Bbs8^{-/-}$ mice displayed a slight reduction in insulin sensitivity which was more evident in females (Supplemental Figure S7G-J). However, this reduction in insulin sensitivity was not significantly affected by *Akap1* heterozygosity. These data demonstrate the contribution of the mitochondria abnormalities to the BBSome deficiency associated defects in glucose metabolism in a manner independent of insulin sensitivity.

3.10. Rescue of the mitochondria defects improves the leptin resistance induced by BBSome deficiency

Leptin resistance is an important underlying mechanism of the obesity and hyperphagia caused by absence of the BBSome [21,24]. Therefore, we examined whether rescuing the mitochondria abnormalities reverses the leptin resistance in BBSome deficient mice. We used phosphorylation of STAT3 as an index of leptin receptor signaling. Relative to vehicle treatment, leptin (2 μg/kg, intraperitoneally) caused a robust increase in phosphorylated STAT3 levels in the hypothalamic arcuate nucleus of control mice (Figure 7N–O). This response was significantly reduced in the $Akap1^{+/+}/Bbs8^{-/-}$ mice, as expected [21]. Interestingly, in $Akap1^{+/-}/Bbs8^{-/-}$ mice, the leptin-induced increase in hypothalamic pSTAT3 was intermediate between control and $Akap1^{+/+}/Bbs8^{-/-}$ mice, suggesting that leptin receptor signaling was partially restored in $Akap1^{+/-}/Bbs8^{-/-}$ mice. This improvement in leptin sensitivity may explain the restoration of energy balance and reduction in adiposity in BBSome deficient mice.

4. DISCUSSION

The current study identifies the BBSome as a new player in the regulation of mitochondria function. We show that loss of the BBSome leads to defects in mitochondrial morphology as indicated by the increased mitochondrial length in cells lacking a functional BBSome. This translates into functional abnormalities as demonstrated by the reduced oxygen consumption rate and the altered mitochondrial distribution and calcium signaling in *Bbs1*KO cells. Mechanistically, we demonstrate that the BBSome modulates the activity of DRP1, a key regulator of mitochondrial fission. Furthermore, we showed that the decrease in DRP1 activity and the defects in the morphology and activity of mitochondria evoked by BBSome deficiency can be rescued through partial loss of AKAP1. Importantly, this was associated with improvements in several of the phenotypes caused by loss of the BBSome such as neuroanatomical abnormalities, obesity and metabolic alterations.

Fusion and fission events are key determinants of mitochondria dynamics that allow this organelle to constantly alter its shape to adjust to cellular and physiological needs [8,9]. Our findings point to the BBSome as a novel modulator of mitochondria dynamic and function by regulating the activity of DRP1, a core component of the canonical mitochondrial fission machinery in mammals. Importantly, re-expression of the *Bbs1* gene rescues the reduction in DRP1 phosphorylation in *Bbs1*KO cells confirming that the effect was due to loss of the *Bbs1* gene. Adaptor proteins recruit DRP1 from the cytosolic compartment to the mitochondrial outer membrane, where it polymerizes into ring- or spiral-shaped superstructures that constrict triggering mitochondrial fission through its GTPase activity [45,46].

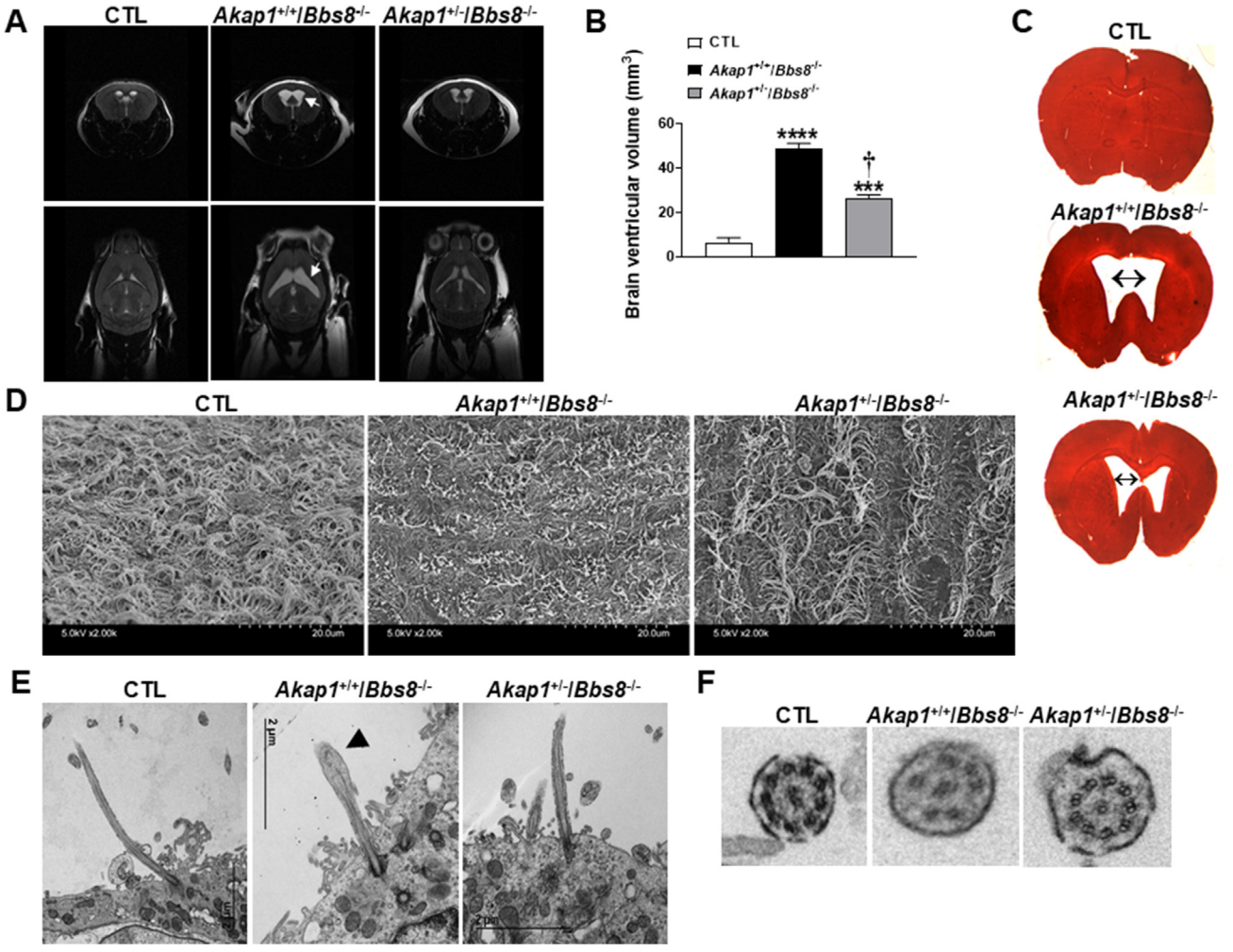

Figure 6: Rescuing the mitochondria defects partially reverses the hydrocephalus associated with BBSome deficiency. (A—B) Representative coronal and sagittal MRI images and quantification of brain ventricles of control (CTL), *Akap1*$^{+/+}$*/Bbs8*$^{-/-}$ and *Akap1*$^{+/-}$*/Bbs8*$^{-/-}$ mice (n = 4/group). The arrow points to the hydrocephalic region. (C) Representative image of neutral-red-stained coronal brain sections of CTL, *Akap1*$^{+/+}$*/Bbs8*$^{-/-}$ and *Akap1*$^{+/-}$*/Bbs8*$^{-/-}$ mice. Double head arrow indicates the enlarged lateral ventricles (n = 2/group). (D) Representative images of scanning electron microscopy of ependymal cell cilia of CTL, *Akap1*$^{+/+}$*/Bbs8*$^{-/-}$ and *Akap1*$^{+/-}$*/Bbs8*$^{-/-}$ mice (n = 3/group). (E) Representative TEM images of ependymal cell cilia of CTL, *Akap1*$^{+/+}$*/Bbs8*$^{-/-}$ and *Akap1*$^{+/-}$*/Bbs8*$^{-/-}$ mice. Arrowhead points to the abnormally swollen cilium. (F) Transverse TEM sections depicting the axonemal arrangement of ciliary microtubules in CTL, *Akap1*$^{+/+}$*/Bbs8*$^{-/-}$ and *Akap1*$^{+/-}$*/Bbs8*$^{-/-}$ mice (n = 3/group). Note, loss of 9 + 2 tubulin structure in *Bbs8*$^{-/-}$ mice was restored in *Akap1*$^{+/-}$*/Bbs8*$^{-/-}$ mice. Data are mean ± SEM and were analyzed with one-way ANOVA. ***P < 0.001, and ****P < 0.0001 vs CTL; †P < 0.0001 vs *Akap1*$^{+/+}$*/Bbs8*$^{-/-}$ mice.

Consistent with the reduced DRP1 activity, *Bbs1*KO cells displayed significant reduction in mitochondrial localization of DRP1. This was further supported by the reduced oxygen consumption rate and altered response to a metabolic challenge (starvation) that depend on DRP1 [33]. Interestingly, our pull-down assay revealed that BBS proteins interact with the CHC which was previously shown to interact with DRP1 [38,39]. We also detected BBSome proteins (BBS7 and BBS8) in isolated mitochondria. However, these proteins were absent in the mitochondria of *Bbs1*KO cells, which indicates that BBS7 and BBS8 do not interact with mitochondria as individual proteins but as part of the BBSome. These findings raise the interesting possibility that in addition to the regulation of DRP1 phosphorylation, the BBSome may be involved in the trafficking or recruitment of DRP1 to the mitochondria membrane. BBSome regulation of DRP1 activity may also involve mechanisms such as ER stress. ER stress has been associated with the control of mitochondria dynamics and DRP1 activity [33,47]. It should be noted that the BBSome component BBS4 was found to localize to the ER and contribute to the ER stress response and trafficking [48]. Moreover, alleviating ER stress partially rescue the BBS phenotypes including photoreceptor degeneration and obesity [49,50]. Additional studies are needed to test each of these possibilities and determine the precise process underlying BBSome regulation of DRP1 activity.

By implicating the BBSome in the regulation of mitochondria function, our findings extend the cellular processes that are regulated by this protein complex. The BBSome is known to play an important role in the regulation of cilia function by mediating the trafficking of cargos to and out of cilia including G protein-coupled receptors and components of intraflagellar transport and other signal transduction pathways [51—53]. Interestingly, our data show that restoration of mitochondria morphology through heterozygous *Akap1* deletion, reverses the ultrastructure changes induced by BBSome deficiency indicating that mitochondria defects underlie the ciliary dysfunction in BBS. Notably, the BBSome has also been implicated in other cellular functions not

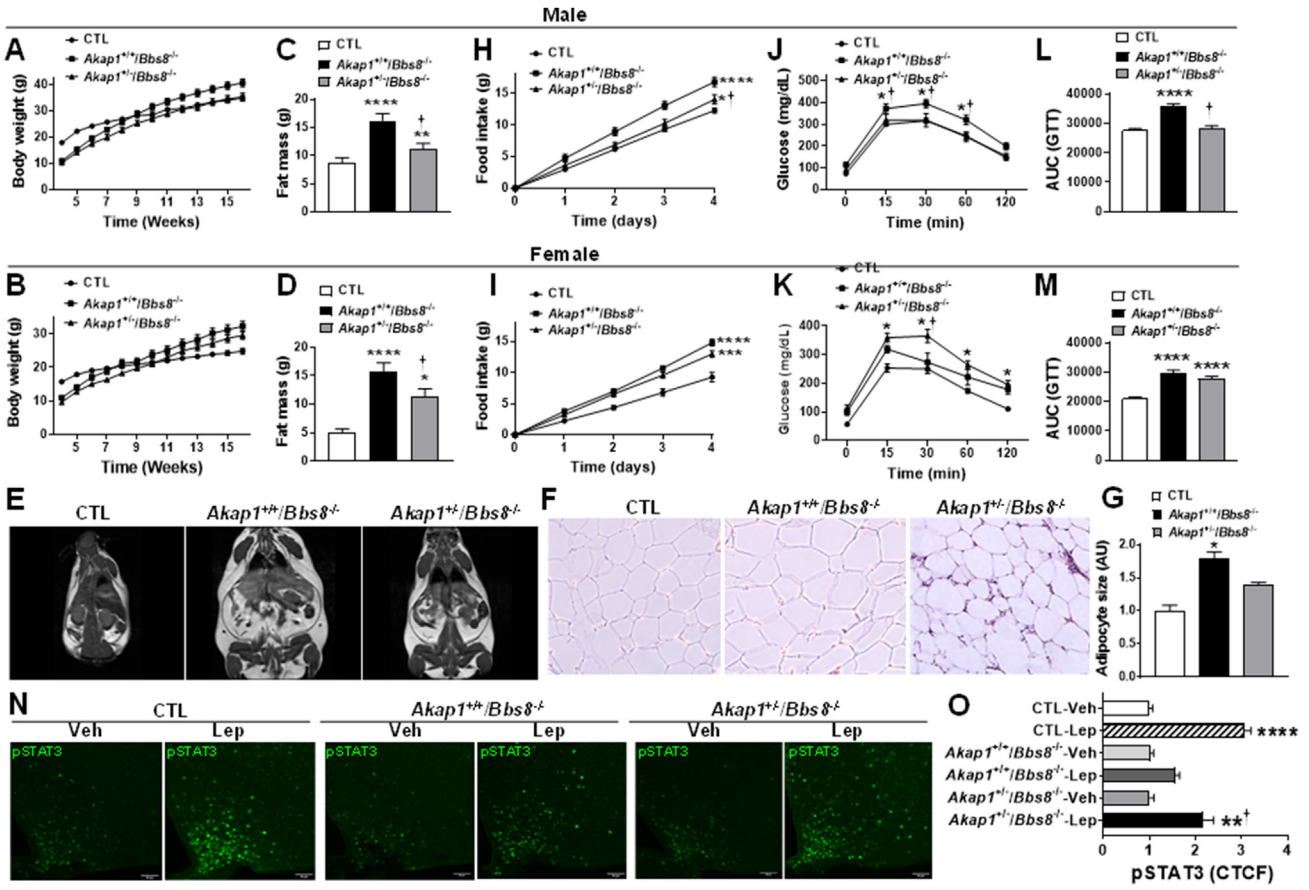

Figure 7: Rescuing the mitochondria defects improves the metabolic abnormalities evoked by BBSome deficiency. (A–D) Body weight and fat mass, obtained by NMR, of male (A, C) and female (B, D) control (CTL; n = 12 male, 13 female), *Akap1*$^{+/+}$*/Bbs8*$^{-/-}$ (n = 14 male, 18 female) and *Akap1*$^{+/-}$*/Bbs8*$^{-/-}$ mice (n = 20 male, 20 female). (E) Representative MRI images of male CTL, *Akap1*$^{+/+}$*/Bbs8*$^{-/-}$ and *Akap1*$^{+/-}$*/Bbs8*$^{-/-}$ mice (n = 3/group). (F–G) Representative images of HE stained white adipose tissue of male CTL, *Akap1*$^{+/+}$*/Bbs8*$^{-/-}$ and *Akap1*$^{+/-}$*/Bbs8*$^{-/-}$ mice (n = 3/group). (H–I) Cumulative food intake of 17 weeks old male (H) and female (I) CTL (n = 12 male, 13 female), *Akap1*$^{+/+}$*/Bbs8*$^{-/-}$ (n = 14 male, 18 female) and *Akap1*$^{+/-}$*/Bbs8*$^{-/-}$ mice (n = 20 male, 20 female). (J–M) Glucose tolerance test (J–K) and area under the curve (AUC, L-M) in male (J, L) and female (K, M) CTL, *Bbs8*$^{-/-}$ and *Akap1*$^{+/-}$*/Bbs8*$^{-/-}$ mice (n = 12/group). (N–O) Representative images (N) and quantification (O) of pSTAT3 immunostaining in the hypothalamic arcuate nucleus in mice treated with vehicle or leptin (2 μg/g bw, IP) (n = 3, 12 images/group). Data are mean ± SEM and were analyzed with repeated measures one-or two-way ANOVA. *P < 0.05, **P < 0.01, ***P < 0.001 and ****P < 0.0001 vs CTL; †P < 0.05 vs *Akap1*$^{+/-}$*/Bbs8*$^{-/-}$ mice.

related to cilia such as sorting of receptors to plasma membrane [20]. For instance, the BBSome interacts with the leptin receptor and mediate its transport to the plasma membrane [21,24]. Consequently, disruption of the BBSome causes leptin resistance resulting in energy imbalance and obesity. Here, we show that rescuing the mitochondria abnormalities significantly reduces the weight gain, adiposity and hyperphagia in BBS mice. This is associated with increased leptin-induced STAT3 activation, indicative of improvement in hypothalamic leptin receptor signaling. Together, these findings implicate mitochondria in the disruption of leptin receptor trafficking and subsequent leptin resistance and obesity in BBS.

Rescue of the BBS-associated ciliary and non-ciliary abnormalities after normalization of mitochondria function in cells points to mitochondrial dysfunction as a unifying mechanism of the cellular and physiological defects evoked by BBSome disruption. This is supported by the fact that alterations in mitochondrial dynamics and function impacts a wide range of cellular processes and have been implicated in numerous human diseases including those commonly associated with BBS such as obesity and neurological problems [3–6]. It should be noted, however, that some of the BBS phenotypes we investigated such as retinal degeneration were not rescued by normalization of mitochondria function. This indicates that the mitochondrial involvement in BBS phenotypes may be cell- or tissue-specific. Future studies are needed to test this possibility.

Taken together, our data demonstrate for the first time that the BBSome is a critical component of the machinery that regulate mitochondria dynamics and function through the control of the activity of DRP1 and point to mitochondrial morphological and functional defects as an important disease mechanism in BBS.

FUNDING

This work was supported by NIH HL084207, VA BX004249, and the University of Iowa Fraternal Order of Eagles Diabetes Research Center to KR; NIH NS125884 to YMU; and NIH HL108932 and VA I01 BX000163 to IMG. The University of Iowa Central Microscopy Research Facility is a core resource supported by the University of Iowa Vice President for Research, and the Carver College of Medicine.

DATA AVAILABILITY

Data will be made available on request.

ACKNOWLEDGMENTS

The authors would like to thank Dr. JianQiang Shao at the University of Iowa Central Microscopy Research Facility for assistance with tissue processing and electron microscopy imaging. We also thank Dr. Renata P. Pereira for the discussion and valuable input on the studies.

CONFLICT OF INTEREST

None declared.

APPENDIX A. SUPPLEMENTARY DATA

Supplementary data to this article can be found online at https://doi.org/10.1016/j.molmet.2022.101654.

REFERENCES

[1] Chaudhuri D, Sancak Y, Mootha VK, Clapham DE. MCU encodes the pore conducting mitochondrial calcium currents. Elife 2013;2:e00704.
[2] Shadel GS, Horvath TL. Mitochondrial ROS signaling in organismal homeostasis. Cell 2015;163(3):560–9.
[3] Liesa M, Shirihai OS. Mitochondrial dynamics in the regulation of nutrient utilization and energy expenditure. Cell Metabol 2013;17(4):491–506.
[4] Norat P, Soldozy S, Sokolowski JD, Gorick CM, Kumar JS, Chae Y, et al. Mitochondrial dysfunction in neurological disorders: exploring mitochondrial transplantation. NPJ Regen Med 2020;5(1):22.
[5] Zhou Z, Austin GL, Young LEA, Johnson LA, Sun R. Mitochondrial metabolism in major neurological diseases. Cells 2018;7(12).
[6] Knott AB, Perkins G, Schwarzenbacher R, Bossy-Wetzel E. Mitochondrial fragmentation in neurodegeneration. Nat Rev Neurosci 2008;9(7):505–18.
[7] Singh A, Faccenda D, Campanella M. Pharmacological advances in mitochondrial therapy. EBioMedicine 2021;65:103244.
[8] Westermann B. Mitochondrial fusion and fission in cell life and death. Nat Rev Mol Cell Biol 2010;11(12):872–84.
[9] Ji WK, Hatch AL, Merrill RA, Strack S, Higgs HN. Actin filaments target the oligomeric maturation of the dynamin GTPase Drp1 to mitochondrial fission sites. Elife 2015;4:e11553.
[10] Franco A, Kitsis RN, Fleischer JA, Gavathiotis E, Kornfeld OS, Gong G, et al. Correcting mitochondrial fusion by manipulating mitofusin conformations. Nature 2016;540(7631):74–9.
[11] Pereira RO, Marti A, Olvera AC, Tadinada SM, Bjorkman SH, Weatherford ET, et al. OPA1 deletion in brown adipose tissue improves thermoregulation and systemic metabolism via FGF21. Elife 2021;10.
[12] Fonseca TB, Sánchez-Guerrero Á, Milosevic I, Raimundo N. Mitochondrial fission requires DRP1 but not dynamins. Nature 2019;570(7761):E34–42.
[13] Cribbs JT, Strack S. Reversible phosphorylation of Drp1 by cyclic AMP-dependent protein kinase and calcineurin regulates mitochondrial fission and cell death. EMBO Rep 2007;8(10):939–44.
[14] Liu Y, Merrill RA, Strack S. A-kinase anchoring protein 1: emerging roles in regulating mitochondrial form and function in health and disease. Cells 2020;9(2).
[15] Merrill RA, Dagda RK, Dickey AS, Cribbs JT, Green SH, Usachev YM, et al. Mechanism of neuroprotective mitochondrial remodeling by PKA/AKAP1. PLoS Biol 2011;9(4):e1000612.
[16] Nachury MV, Loktev AV, Zhang Q, Westlake CJ, Peränen J, Merdes A, et al. A core complex of BBS proteins cooperates with the GTPase Rab8 to promote ciliary membrane biogenesis. Cell 2007;129(6):1201–13.
[17] Nachury MV, Seeley ES, Jin H. Trafficking to the ciliary membrane: how to get across the periciliary diffusion barrier? Annu Rev Cell Dev Biol 2010;26:59–87.
[18] Green JS, Parfrey PS, Harnett JD, Farid NR, Cramer BC, Johnson G, et al. The cardinal manifestations of Bardet-Biedl syndrome, a form of Laurence-Moon-Biedl syndrome. N Engl J Med 1989;321(15):1002–9.
[19] Sheffield VC, Nishimura D, Stone EM. The molecular genetics of Bardet-Biedl syndrome. Curr Opin Genet Dev 2001;11(3):317–21.
[20] Zhao Y, Rahmouni K. BBSome: a new player in hypertension and other cardiovascular risks. Hypertension 2022;79(2):303–13.
[21] Guo DF, Cui H, Zhang Q, Morgan DA, Thedens DR, Nishimura D, et al. The BBSome controls energy homeostasis by mediating the transport of the leptin receptor to the plasma membrane. PLoS Genet 2016;12(2):e1005890.
[22] Guo DF, Lin Z, Wu Y, Searby C, Thedens DR, Richerson GB, et al. The BBSome in POMC and AgRP neurons is necessary for body weight regulation and sorting of metabolic receptors. Diabetes 2019;68(8):1591–603.
[23] Wang L, Liu Y, Stratigopoulos G, Panigrahi S, Sui L, Zhang Y, et al. Bardet-Biedl syndrome proteins regulate intracellular signaling and neuronal function in patient-specific iPSC-derived neurons. J Clin Invest 2021;131(8).
[24] Seo SJ, Guo DF, Bugge K, Morgan DA, Rahmouni K, Sheffield VC. Requirement of Bardet-Biedl syndrome proteins for leptin receptor signaling. Hum Mol Genet 2009;18(7):1323–31.
[25] Flippo KH, Gnanasekaran A, Perkins GA, Ajmal A, Merrill RA, Dickey AS, et al. AKAP1 protects from cerebral ischemic stroke by inhibiting drp1-dependent mitochondrial fission. J Neurosci 2018;38(38):8233–42.
[26] Rahmouni K, Fath MA, Seo S, Thedens DR, Berry CJ, Weiss R, et al. Leptin resistance contributes to obesity and hypertension in mouse models of Bardet-Biedl syndrome. J Clin Invest 2008;118(4):1458–67.
[27] Hsu Y, Garrison JE, Kim G, Schmitz AR, Searby CC, Zhang Q, et al. BBSome function is required for both the morphogenesis and maintenance of the photoreceptor outer segment. PLoS Genet 2017;13(10):e1007057.
[28] Seo S, Mullins RF, Dumitrescu AV, Bhattarai S, Gratie D, Wang K, et al. Subretinal gene therapy of mice with Bardet-Biedl syndrome type 1. Invest Ophthalmol Vis Sci 2013;54(9):6118–32.
[29] López-Doménech G, Higgs NF, Vaccaro V, Roš H, Arancibia-Cárcamo IL, MacAskill AF, et al. Loss of dendritic complexity precedes neurodegeneration in a mouse model with disrupted mitochondrial distribution in mature dendrites. Cell Rep 2016;17(2):317–27.
[30] Rysted JE, Lin Z, Walters GC, Rauckhorst AJ, Noterman M, Liu G, et al. Distinct properties of Ca(2+) efflux from brain, heart and liver mitochondria: the effects of Na(+), Li(+) and the mitochondrial Na(+)/Ca(2+) exchange inhibitor CGP37157. Cell Calcium 2021;96:102382.
[31] Starks RD, Beyer AM, Guo DF, Boland L, Zhang Q, Sheffield VC, et al. Regulation of insulin receptor trafficking by Bardet biedl syndrome proteins. PLoS Genet 2015;11(6):e1005311.
[32] Watters O, Connolly NMC, König HG, Düssmann H, Prehn JHM. AMPK preferentially depresses retrograde transport of axonal mitochondria during localized nutrient deprivation. J Neurosci 2020;40(25):4798–812.
[33] Santoro A, Campolo M, Liu C, Sesaki H, Meli R, Liu ZW, et al. DRP1 suppresses leptin and glucose sensing of POMC neurons. Cell Metabol 2017;25(3):647–60.
[34] Koval OM, Nguyen EK, Santhana V, Fidler TP, Sebag SC, Rasmussen TP, et al. Loss of MCU prevents mitochondrial fusion in G(1)-S phase and blocks cell cycle progression and proliferation. Sci Signal 2019;12(579).
[35] Nguyen EK, Koval OM, Noble P, Broadhurst K, Allamargot C, Wu M, et al. CaMKII (Ca(2+)/calmodulin-dependent kinase II) in mitochondria of smooth muscle cells controls mitochondrial mobility, migration, and neointima formation. Arterioscler Thromb Vasc Biol 2018;38(6):1333–45.
[36] Kumar Sharma R, Chafik A, Bertolin G. Mitochondrial transport, partitioning, and quality control at the heart of cell proliferation and fate acquisition. Am J Physiol Cell Physiol 2022;322(2):C311–25.
[37] Langousis G, Shimogawa MM, Saada EA, Vashisht AA, Spreafico R, Nager AR, et al. Loss of the BBSome perturbs endocytic trafficking and disrupts virulence of Trypanosoma brucei. Proc Natl Acad Sci U S A 2016;113(3):632–7.

[38] Bednarek SY, Backues SK. Plant dynamin-related protein families DRP1 and DRP2 in plant development. Biochem Soc Trans 2010;38(3):797—806.
[39] Yoshinari A, Fujimoto M, Ueda T, Inada N, Naito S, Takano J. DRP1-Dependent endocytosis is essential for polar localization and boron-induced degradation of the borate transporter BOR1 in Arabidopsis thaliana. Plant Cell Physiol 2016;57(9):1985—2000.
[40] Edwards G, Perkins GA, Kim KY, Kong Y, Lee Y, Choi SH, et al. Loss of AKAP1 triggers Drp1 dephosphorylation-mediated mitochondrial fission and loss in retinal ganglion cells. Cell Death Dis 2020;11(4):254.
[41] Mykytyn K, Mullins RF, Andrews M, Chiang AP, Swiderski RE, Yang B, et al. Bardet-Biedl syndrome type 4 (BBS4)-null mice implicate Bbs4 in flagella formation but not global cilia assembly. Proc Natl Acad Sci U S A 2004;101(23):8664—9.
[42] Fath MA, Mullins RF, Searby C, Nishimura DY, Wei J, Rahmouni K, et al. Mkks-null mice have a phenotype resembling Bardet-Biedl syndrome. Hum Mol Genet 2005;14(9):1109—18.
[43] Davis RE, Swiderski RE, Rahmouni K, Nishimura DY, Mullins RF, Agassandian K, et al. A knockin mouse model of the Bardet-Biedl syndrome 1 M390R mutation has cilia defects, ventriculomegaly, retinopathy, and obesity. Proc Natl Acad Sci U S A 2007;104(49):19422—7.
[44] Guo DF, Rahmouni K. Molecular basis of the obesity associated with Bardet-Biedl syndrome. Trends Endocrinol Metabol 2011;22(7):286—93.
[45] Losón OC, Song Z, Chen H, Chan DC. Fis1, mff, MiD49, and MiD51 mediate Drp1 recruitment in mitochondrial fission. Mol Biol Cell 2013;24(5):659—67.
[46] Liu R, Chan DC. The mitochondrial fission receptor Mff selectively recruits oligomerized Drp1. Mol Biol Cell 2015;26(24):4466—77.
[47] Marchi S, Patergnani S, Pinton P. The endoplasmic reticulum-mitochondria connection: one touch, multiple functions. Biochim Biophys Acta 2014;1837(4):461—9.
[48] Anosov M, Birk R. Bardet-Biedl syndrome obesity: BBS4 regulates cellular ER stress in early adipogenesis. Mol Genet Metabol 2019;126(4):495—503.
[49] Drack AV, Dumitrescu AV, Bhattarai S, Gratie D, Stone EM, Mullins R, et al. TUDCA slows retinal degeneration in two different mouse models of retinitis pigmentosa and prevents obesity in Bardet-Biedl syndrome type 1 mice. Invest Ophthalmol Vis Sci 2012;53(1):100—6.
[50] Mockel A, Obringer C, Hakvoort TB, Seeliger M, Lamers WH, Stoetzel C, et al. Pharmacological modulation of the retinal unfolded protein response in Bardet-Biedl syndrome reduces apoptosis and preserves light detection ability. J Biol Chem 2012;287(44):37483—94.
[51] Berbari NF, Lewis JS, Bishop GA, Askwith CC, Mykytyn K. Bardet-Biedl syndrome proteins are required for the localization of G protein-coupled receptors to primary cilia. Proc Natl Acad Sci U S A 2008;105(11):4242—6.
[52] Loktev AV, Jackson PK. Neuropeptide Y family receptors traffic via the Bardet-Biedl syndrome pathway to signal in neuronal primary cilia. Cell Rep 2013;5(5):1316—29.
[53] Williams CL, McIntyre JC, Norris SR, Jenkins PM, Zhang L, Pei Q, et al. Direct evidence for BBSome-associated intraflagellar transport reveals distinct properties of native mammalian cilia. Nat Commun 2014;5:5813.

